A Novel Approach for Designing a Sub-Bandgap in CuGa(S,Te)$_2$ Thin Films Assisted with Numerical Simulation of Solar Cell Devices for Photovoltaic Application

Karthikeyan Vijayan, Logu Thirumalaisamy, Srikarumbur Pandurangan Vijayachamundeeswari,* Kalainathan Sivaperuman, Nazmul Ahsan, and Yoshitaka Okada

ACCESS | Metrics & More | Article Recommendations

ABSTRACT: As a well-explored chalcopyrite material, copper gallium sulfide CGS has been considered a potential material for solar cell absorber layers. However, its photovoltaic attributes still require to be improved. In this research, a novel chalcopyrite material, copper gallium sulfide telluride CGST, has been deposited and verified as a thin film absorber layer to fabricate high-efficiency solar cells by experimental testing and numerical simulations. The results display the intermediate band formation in CGST with incorporation of Fe ions. Electrical studies showed enhancement in mobility from 1.181 to 1.473 cm^2 V^{-1} s^{-1} and conductivity from 2.182 to 5.952 S cm^{-1} for pure and 0.08 Fe-substituted thin films. The $I-V$ curves display the photoresponse and ohmic nature of the deposited thin films, and the maximum photoresponsivity (0.109 A W^{-1}) was observed for 0.08 Fe-substituted films. Theoretical simulation of the prepared solar cells was carried out using SCAPS-1D software, and the obtained efficiency displayed an increasing trend from 6.14 to 11.07% as the Fe concentration increased from 0.0 to 0.08. This variation in efficiency is attributed to the decrease in bandgap (2.51−1.94 eV) and the formation of an intermediate band in CGST with Fe substitution, which is evidenced in UV−vis spectroscopy. The above revealed results open the way to 0.08 Fe-substituted CGST as a promising candidate as a thin film absorber layer in solar photovoltaic technology.
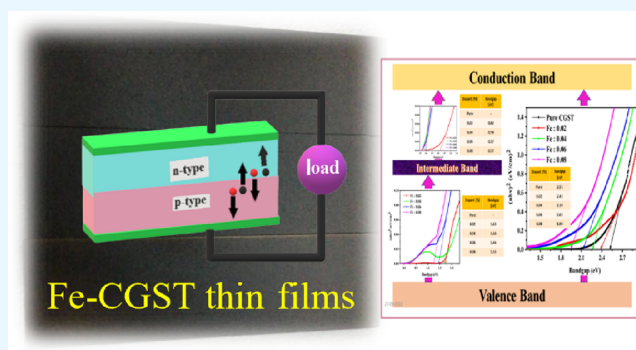
1. INTRODUCTION

The prompt increase in the human population and industrial development results in an enormous rise in the energy crisis, which drives us to search unconventional, environment-friendly, and renewable energy sources. The infinite solar energy source is the most promising route to overcome this energy crisis.[1] Principally, the solar cell efficiency depends on the recombination rate of electron−hole pairs and the absorbance region in the solar spectra. Hence, broadening the absorption region to improve the attributes of the primary layers (i.e., absorber and window layer) is a practical analysis for achieving high-efficiency conversion.[2] As a part of this route, the concept of the intermediate band (IB) in wide-bandgap semiconductor materials was introduced. IB solar cells have increased attention owing to their higher efficiency by developing the impurity energy levels between the valence and conduction bands, which absorb lower energy photons. About 63.1% of maximum theoretical efficiency was estimated for the intermediate band solar cell (IBSC) under one sunlight energy.[3,4] In the IB solar cells, the material that possesses the IB is placed amid the n-type and p-type semiconductors, as

shown in Figure 1. For such material, the sub-bandgap energy photons are captured by the transitions from the valence band (VB) to the IB and then from the IB to the conduction band (CB). These collectively give the current, which can be generated in the conventional photon absorption from the VB to the CB. The IB can also be considered as a set of two series of cells corresponding to the VB−IB and IB−CB transitions and one in parallel, corresponding to the VB−CB transition. These can give the IB solar cell additional property to harvest the solar spectrum.[5]

Photons can pump electrons from the VB to the CB when sunlight irradiates the solar cell. During this process, the first photon triggers the electron from the VB to the IB and then
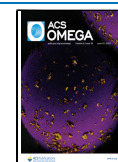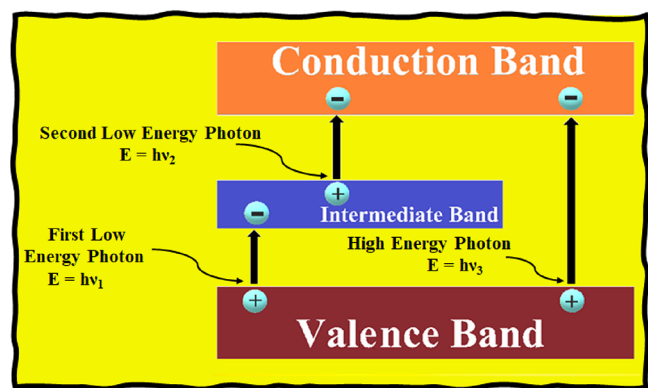
Figure 1. Schematic diagram of the intermediate band in the semiconductor and the transition mechanism of the IB in the semiconductor.

from the IB to the CB. The electrons can be excited not just by a single high-energy photon but can also be made likely by two low-energy photons. Since the above-described process occurs in addition to the usual pushing of electrons from the VB to the CB by photons with energy much higher than that of the band gap, the photocurrent generated by the solar cell could be more than that in the case of a conventional type.[4] Gaur et al. attempted to create an IB gap in $CuAlS_2$ to improve its absorption in visible light and power conversion efficiency for solar cell applications. The work succeeded in its aim by incorporating Sn/Fe in the $CuAlS_2$ thin films.[6] Pérez et al. investigated PbTe/CdTe, PbSe/ZnTe, and InN/GaN to reveal the best one to attain an efficiency near the theoretical limit of the IBSCs. The analysis displayed that the performance of SC can be enhanced by varying the quantum dots and obtaining a maximum efficiency of 59.78% for PbSe/ZnTe QDs.[7] Peng et al. scrutinized the effect of the metallic IB in Cr-doped $AgGaS_2$ by first principles and then analyzed it by experimental steps. The enhanced optical absorption coefficients in the visible range affirmed the potential candidacy of Cr-doped $AgGaS_2$ with IB in solar cell applications.[8] Guillén and Herrero discussed the impact of copper on the physical attributes of $Cu_xGaCr_{0.1}S_2$ thin films for IBSC. The study revealed that the presence of Cr showed an in-gap absorption independent of the Cu/Ga ratio. The increased electrical conductivity with the Cu content displayed its effectiveness in solar cell applications.[9] Fan et al. assessed the optical characteristics of Sn-$CuGaSe_2$ thin films and optimized their effectiveness in the solar cell due to the presence of the IB. The band gap of $CuGa_{1-x}Sn_xSe_2$ thin films was tuned from 1.65 to 1.41 eV for the doping content from 0.00 to 0.06, which confirmed the formation of the IB, which leads to low-energy photon absorption.[10] Lv et al. disclosed the effect of the IB in increasing solar cell efficiency by incorporating Ti in CGS_2. Photoelectrochemical analysis of the material proved the solar response in the presence of the IB, which leads to low-energy photon absorption, and thereby verified it as an appreciable solar cell candidate.[11] Copper gallium sulfide telluride (CGST) is a quaternary material from the chalcogenide family containing earth-abundant compounds and has a wide band gap with a high absorption coefficient.[12] CGST is an ideal host for IB materials owing to its wide-range band gap of 2.43 eV.[13] Electronic band structure calculations based on first principles have verified the feasibility of the concept of IBSC.[14] Numerous theoretical studies on doping transition metals on

chalcopyrite reported IBSC for photovoltaics. Formerly, Ti-$CuGaS_2$,[11] Mn-$CuGaS_2$,[15] and Cr-$CuGaS_2$[16,17,30] IB materials were also suggested with partial substitution of dopants for Ga. In the context of Fe, the idea of 0.92 and 1.54 eV transitions, along with a 2.46 eV band gap, theoretically leads to efficiencies of 47% at ideal circumstances under one sun illumination.[18] There are many experimental reports on the optical characteristics of $CuGaS_2$:Fe crystals, relating diverse absorption attributes at 1.2 and 1.9 eV due to the Fe occurrence.[19]

In the present research, we state the IB formation in chalcogenide structure CGST thin films by substituting Fe. The $CuGa_{1-x}Fe_x(S, Te)_2$ thin films were deposited via the spray pyrolysis route by varying the atomic ratio of Ga/Fe. To our knowledge, there are no reports on using this technique to fabricate IB thin films. The impact of Fe integration on the electrical, structural, and optical characteristics is scrutinized and compared with that of pristine CGST. The electrical characterizations displayed the enhancement in mobility from 1.181 to 1.473 cm^2 V^{-1} s^{-1} and conductivity from 2.182 to 5.952 S cm^{-1} for pure and Fe-0.08-substituted thin films. The maximum photoresponsivity (0.109 A W^{-1}) and sub-band were observed for 0.08 Fe-substituted films, which possess potential application in solar photovoltaics. Moreover, the study attempted to stimulate CIGS/Si solar cells using the SCAPS 1-D simulator. The work utilized the experimentally obtained data as some parameters for the SCAPS 1-D software. It analyzed the photovoltaic characteristics of the simulated solar cells and the obtained photovoltaic attributes appreciably complimenting the experimental data.

2. EXPERIMENTAL PROCEDURE

Pure and Fe-incorporated CGST thin films were deposited on the soda-lime glass substrate using the chemical spray pyrolysis technique. The dopant percentage varied from 0.02 to 0.08. Copper(II) chloride ($CuCl_2 \cdot 2H_2O$) in 0.1 M, gallium(III) nitrate ($3Ga(NO_3)_3 \cdot 9H_2O$), thiourea (CH_4N_2S), and ferric nitrate ($FeH_{18}N_3O_{18}$) were weighed and taken separately and dissolved in double-distilled water. Tellurium dioxide (TeO_2) and hydrogen chloride (HCl) were used as a Te source and a reducing agent, respectively. Then, they were mixed at their required ratio to have a stoichiometric solution. First, $CuCl_2 \cdot 2H_2O$ and $3Ga(NO_3)_3 \cdot 9H_2O$ were mixed and then the TeO_2 and $FeH_{18}N_3O_{18}$ solution was added. Finally, the prepared solution was mixed with the CH_4N_2S solution. Before deposition, the substrates were cleaned ultrasonically using Millipore water and acetone separately. The temperature of the substrate was fixed at 250 °C, the nozzle to substrate distance was maintained at 24 cm, and the 60 mL of the precursor solution was sprayed. At a substrate temperature of 250 °C, the solvent evaporated before the droplet reached the substrate. Then, the pure and Fe-incorporated CGST melted, precipitated, vaporized in the atmosphere without decomposition, and was deposited in the substrate.[20] Figure 2 represents the schematic route of the synthesis process of Fe-substituted CGST thin films.

2.1. Device Simulation and Structure. Figure 3 depicts the schematic representation of the solar cell inspected in this research with its elements glass/Fe-CGST/In_2S_3/AZO. The method to attain suitable efficiency is utilizing numerical simulations to study the solar cell attributes and its photovoltaic performance. Table 1 shows the parameters of the simulated solar. The structure of the solar cell is assessed
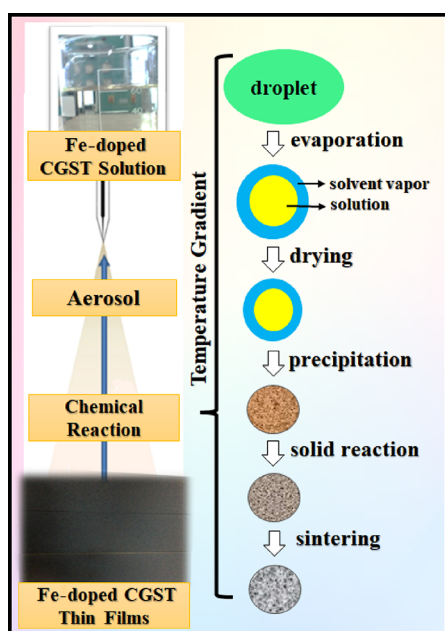
Figure 2. Schematic route of the synthesis process of Fe-substituted CGST thin films.
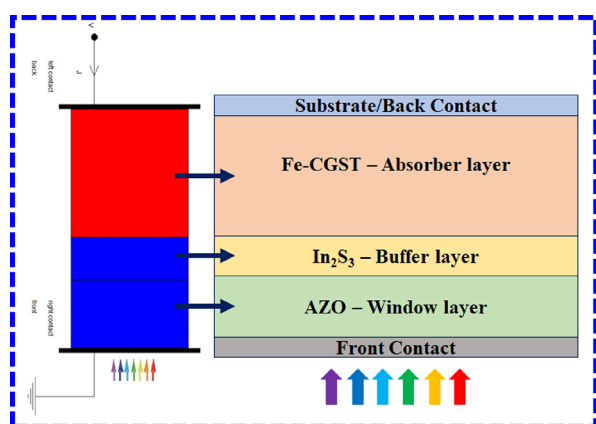

Figure 3. The schematic diagram of solar cell structure.

Table 1. Base Parameters for the Simulation of $CG_{1-x}Fe_xST/In_2S_3/AZO$ Heterojunction Solar Cell Structures[34−37]

layer parameters	CGST	In_2S_3	AZO
layer thickness	1.5 μm	500 nm	800 nm
electron affinity (eV)	4.5	4.7	4.6
layer band gap (eV)	2.51−1.90	2.1	3.3
dielectric relative permittivity	13.6	13.5	9
effective conduction band state density (cm^{-3})	2.2×10^{18}	1.8×10^{19}	2.2×10^{18}
effective valence band state density (cm^{-3})	1.8×10^{19}	4.0×10^{13}	1.8×10^{19}
electron thermal velocity (V_e)	1×10^7		
hole thermal velocity (V_n)	1×10^7		
electron mobility (cm^2/V·s)	1.0×10^2	4.0×10^2	1×10^2
hole mobility (cm^2/V·s)	2.5×10^1	2.1×10^2	2.5×10^1
doping concentration of donors (cm^{-3})	0	1×10^{18}	1×10^{18}
doping concentration of acceptors (cm^{-3})	2×10^{16}	1×10^1	0

under a AM 1.5 solar spectrum, incident light power $P = 1000$ W·m^{-2}, and temperature $T = 300$ K. We provided the attained results, postulating the varied and constant parameters during the simulation. The optimized parameters (back contact, absorber layer, buffer layer, window layer, and front contact) were obtained from the literature.[31−33]

3. CHARACTERIZATION

The structural confirmation of thin films was studied using X-ray diffraction patterns and was obtained using a Bruker X-8 X-ray diffractometer (Cu Kα1 radiation, λ = 1.54056 Å), operating at 40 kV and 30 mA. The surface uniformity was analyzed from the thin film's micro-Raman spectrum and obtained via a Horiba Jobin-Yvon LabRam HR800 spectrometer. The surface morphology of deposited films was assessed using an EVO 18 Research, Carl Zeiss scanning electron microscope and an atomic force microscope from Nanosurf easyScan 2, Nanosurf AG, Switzerland). The elemental studies were investigated using an energy-dispersive X-ray spectroscope (EDS, Bruker Nano) and an XPS Kratos AXIS-165 instrument using a Monochromatic Al Kα radiation source. The optical attributes were characterized in the wavelength range 200−2500 nm using a UV−vis−NIR spectrophotometer (Jasco V-670 PC). The electrical aspects of the films were investigated using a Hall measurement setup (Ecopia HMS-3000) in the van der Pauw configuration. Current−voltage curves were analyzed using Princeton EG&G.

4. RESULTS AND DISCUSSION

4.1. Optical Analysis. *4.1.1. UV−Visible Spectroscopy.* The research attempted to introduce an IB gap to enhance the solar cell efficiency compared to reported works. The formation of IB was assessed and confirmed using UV−vis spectroscopy. Figure 4 represents the absorption spectra for
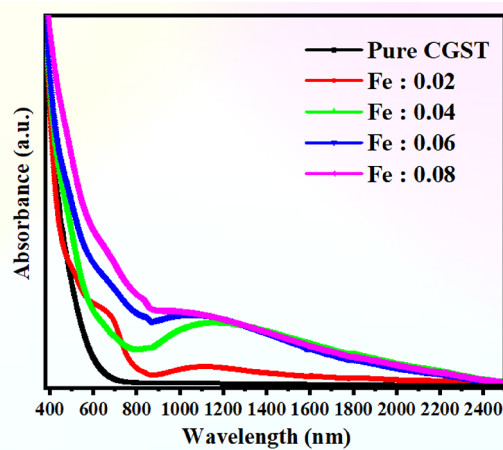

Figure 4. UV absorption spectra of pure CGST and Fe-substituted CGST (0.02−0.08) thin films.

pure and doped thin films. The optical absorption increases with an increase in the Fe dopant ratio. Therefore, doped thin films show a redshift compared to pure CGST thin films. The Fe 0.08-doped CGST thin film showed a stretched redshift (59 nm). The absorption edge of the redshift in Fe-doped CGST has been ascribed to the transition of charge transfer between Fe^{3+} and the CGST CB or VB. The transitions from the VB to the intermediate and CB can efficiently reach the redshift band
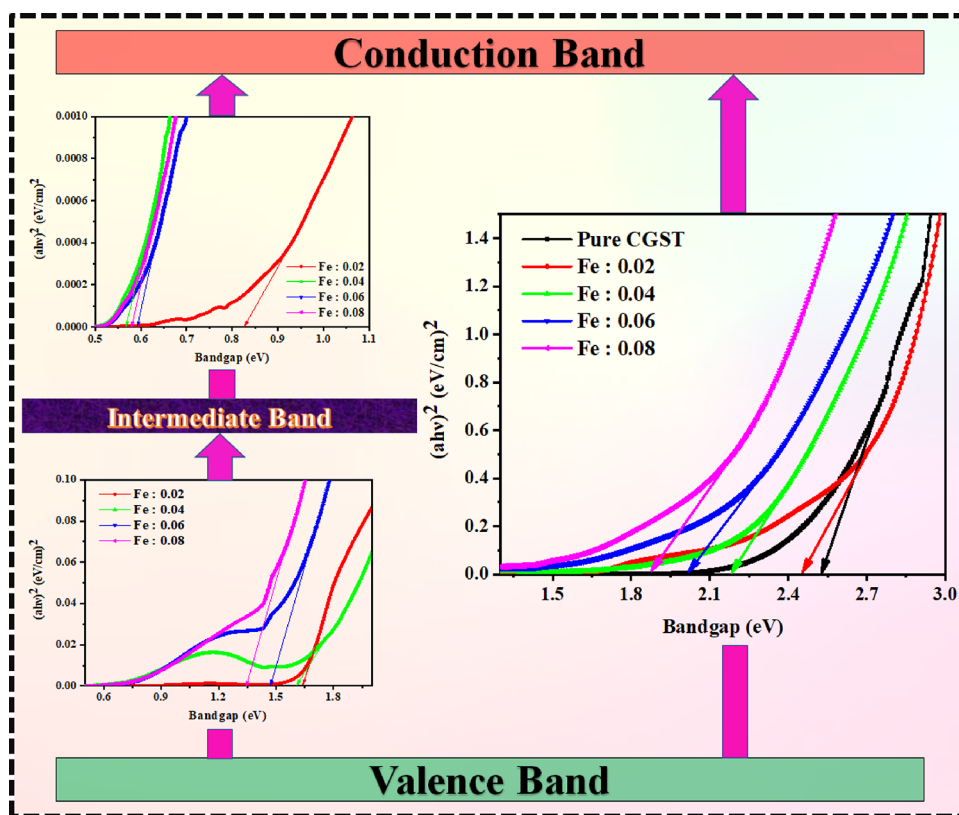
Figure 5. Optical band gap plot for pure and Fe-substituted CGST (0.02−0.08) thin films.

edge absorption threshold. The redshift is because of the extension of the carriers between the VB and CB.

The optical band gap was calculated via the Tauc plot relation shown in Figure 5, and the calculated values are tabulated in Table 2. The determined band gap of the

Table 2. Calculated Bandgap Values and Roughness (RMS Value) for Pure CGST and Fe-Substituted CGST Thin Films

sample name	band gap (VB to CB) eV	band gap (VB to IB) eV	band gap (IB to CB) eV	roughness (RMS value) nm
pure CGST	2.51			28.8
Fe 0.02	2.45	1.63	0.82	40.18
Fe 0.04	2.19	1.60	0.59	34.69
Fe 0.06	2.03	1.46	0.57	22.73
Fe 0.08	1.90	1.33	0.57	15.58

deposited CGST thin film is obtained as 2.51 eV. The band gap decreases from 2.51 eV (pure CGST) to 1.94 eV (Fe 0.08), respectively. This band-gap reduction is due to the states driven by the Fe substitution near the VB of the CGST system. The IB is observed for Fe-substituted thin films in the substitution ratio of 0.2 to 0.8%. Generally, IB formation occurs when transition metals are added to the CGST system. The presence of transition metals hybridizes the 3d valence electrons of CGST, thereby increasing the absorption coefficient and developing the IB. It is possible to add a partially filled IB that allows for three-photon transitions (from the VB to the IB, from the IB to the CB, and also from the VB to the CB), allowing for greater photocurrents without compromising photovoltage. Marti and Luque proposed the

introduction of a partially filled IB in the primary prohibited band gap of a wide band gap semiconductor in 1997 to transcend the SQ limit on single-junction solar cells.[28] V.Suba et al. studied the theoretical investigation of crystal field theory (CFT) for Fe-CGS thin films, revealing the tetrahedral field. The IB observation is primarily associated with breaking Fe 3d degeneracy states in the CGST system. Henceforth, in tetrahedral material, 3d states are divided into two dominant folds, namely, t_2 (higher energy state) and e (lower energy state). The distance between the states is the minimum for a high spin and the maximum for a low spin. The possibility of the formation of the IB is high due to the high spin state in the CGST system.[2] The present experimental research satisfies these conditions, and some of the dopants (Fe, Cr, Ti) showed similar results for confirmation of the IB in the CGS system.[29,19,16] In summary, the increase in Fe substitution in CGST also increases IB absorption in the visible region. Due to the increase in the absorption spectra for the absorber layer, the conversion efficiency of the solar cell will also be enhanced.

4.1.2. Photoluminescence Spectroscopy. The photoluminescence (PL) study was carried out for pure and Fe 0.08-substituted CGST thin films, shown in Figure 6. The diode laser (405 nm) was used to excite the deposited thin films at room temperature. The major PL peak was observed at ∼509 nm for pure and ∼650 nm for Fe 0.08-substituted CGST thin films. An additional broad PL peak at ∼920 nm was also observed for Fe 0.08-substituted CGST thin films. PL emission is directly related to the recombination of excited electrons and holes. The recombination rate and effective charge transfer in the Fe-incorporated CGST thin films compared to the pure CGST thin film suggested the presence of an IB in Fe-incorporated CGST thin films. Due to the presence of the IB,
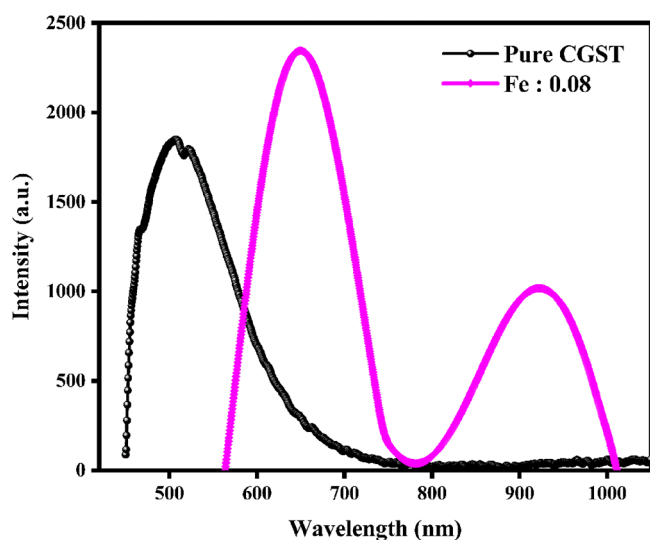
Figure 6. PL spectra of pure CGST and Fe 0.08-substituted CGST thin films.

the efficiency of the device might increase, which makes it a potential applicant for solar cells.

4.2. Electrical Analysis. *4.2.1. Hall Effect Analysis.* The formation of an IB gap facilitates an increase in electrical aspects of samples, and the electrical attributes of pristine and Fe-CGST thin films were analyzed via Hall effect analysis using a four-probe technique at room temperature. Figure 7a−d shows the conductivity, resistivity, mobility, and carrier concentration variations of pure and Fe-substituted CGST thin films. The deposited thin films showed p-type conductivity due to the positive Hall coefficient. The variations in carrier concentration, resistivity, mobility, and conductivity

measurement values of pristine CGST and Fe-substituted CGST thin films are shown in Table 3. The deficiency of Cu ions leads to metal vacancies in pure CGST lattice and turns them into acceptors. This deficiency of Cu could be the motive for the p-type conductivity nature. The carrier concentration is decreasing compared to pure thin films due to the ionized impurity scattering of Fe substitution. When the Fe substitution percentage increased, the mobility increased from 1.181 to 1.736 cm^2 V^{-1} s^{-1} compared to pure CGST thin films. This enhancement is because of less boundary scattering confirmed by AFM and XRD studies. The increased crystallite size gives lower-density grain boundaries, which act as carriers' traps and barriers for carrier transport and enhance the carrier's lifetime. Moreover, the substitution of Fe into the Ga site gives consistent variation in all electrical parameters of the deposited thin films. Significantly, the conductivity of the deposited film has improved from 2.182 S cm^{-1} (pure CGST) to 5.952 S cm^{-1} (Fe 0.08). The resistivity of the deposited thin films depends on the high crystalline nature; here, for pure (4.582 ohm-cm) and Fe 0.08 (1.68 ohm-cm), there is a decrease in resistance and lattice strain due to the fewer grain boundaries.

4.2.2. I−V Measurements. The I−V measurement in light and dark illumination conditions determines the ohmic nature of pure CGST and Fe-substituted CGST thin films, as shown in Figure 8. The photoresponsivity and photocurrent depend on the dopant percentage of the deposited pure CGST and Fe-substituted thin films under certain conditions to define its potential to use as an absorber layer for photovoltaic solar cell applications. The electrical contacts (silver-coated) were employed on the pure and Fe-substituted thin films, and the contacts were connected in series with a pico-ammeter and power supply. The prepared thin films were subjected to a
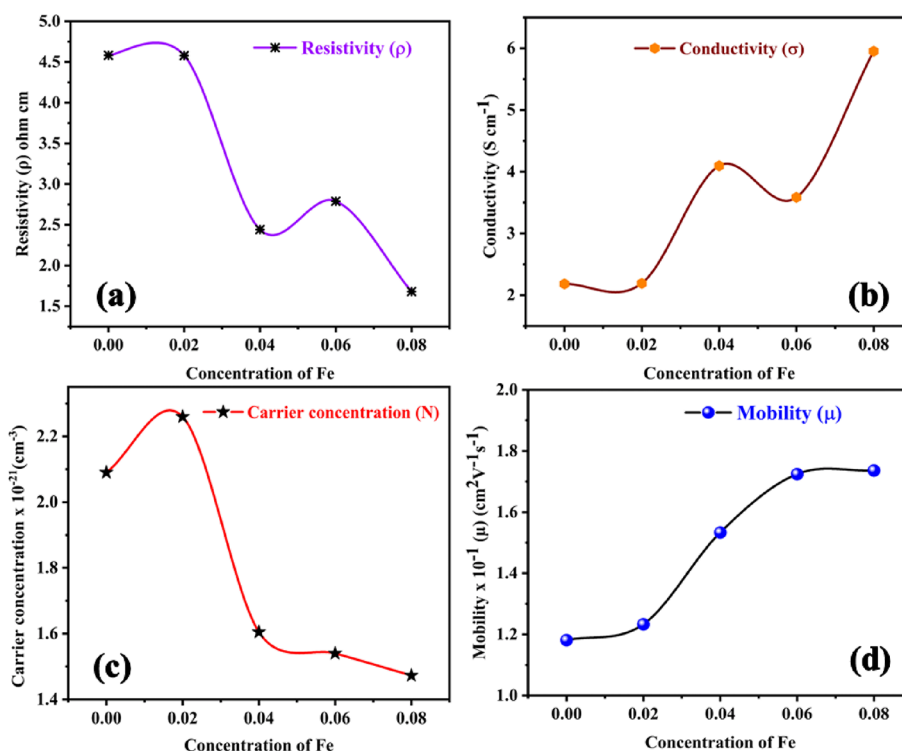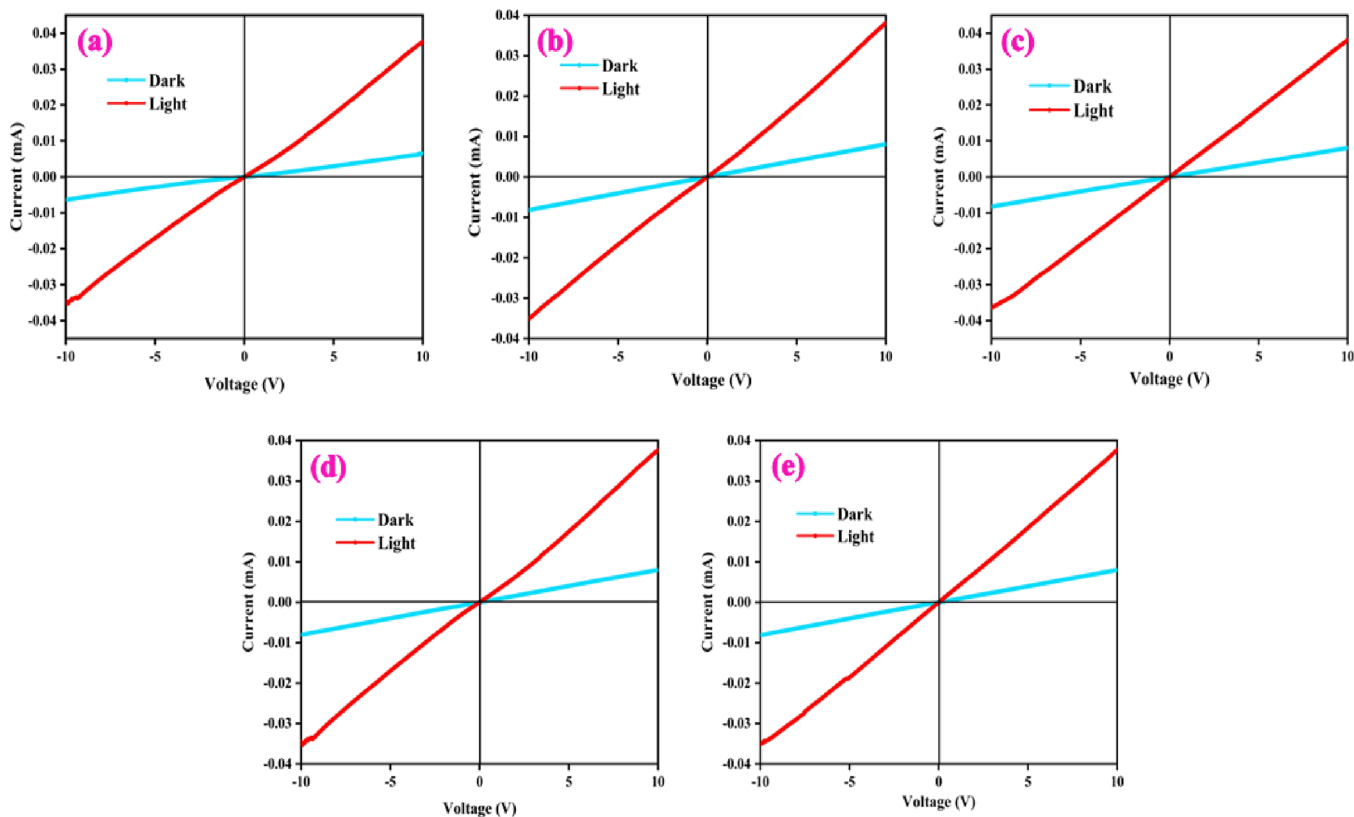

Figure 7. Hall measurements plot for (a) resistivity vs. Fe concentration. (b) Conductivity vs. Fe concentration. (c) Carrier concentration vs. Fe concentration. (d) Mobility vs. Fe concentration of pure CGST and Fe-substituted CGST thin films.

Table 3. Variation in Carrier Concentration, Mobility, Resistivity, and Conductivity of Pure CGST and Fe-Substituted CGST Thin Films

sample name	conduction type	carrier concentration $\times 10^{21}$ (cm^{-3})	mobility $\times 10^{-1}$ (cm^2 V^{-1} s^{-1})	resistivity (Ω cm)	conductivity (S cm^{-1})
pure CGST	P	2.090	1.181	4.582	2.182
Fe 0.02	P	2.259	1.233	4.590	2.190
Fe 0.04	P	1.605	1.533	2.582	4.095
Fe 0.06	P	1.540	1.724	2.779	3.584
Fe 0.08	P	1.473	1.736	1.680	5.952

Figure 8. $I-V$ characteristics of (a) pure CGST thin films with different concentrations of (b) Fe 0.02, (c) Fe 0.04, (d) Fe 0.06, and (e) Fe 0.08.

Table 4. Photoresponsivity and Photocurrent for Pure and Fe-Substituted CGST (0.02−0.08) Thin Films with a Bias Voltage (10 V)

sample name	I_L (under light) (A)	I_D (under dark) (A)	photocurrent (A)	photoresponsivity (A W^{-1})
CGST pure	3.81×10^{-2}	8.09×10^{-3}	3.0×10^{-2}	0.001
Fe 0.02	3.80×10^{-2}	8.09×10^{-3}	2.9×10^{-2}	0.0011
Fe 0.04	3.76×10^{-2}	8.01×10^{-3}	2.9×10^{-2}	0.0011
Fe 0.06	3.50×10^{-2}	8.10×10^{-3}	2.6×10^{-2}	0.0104
Fe 0.08	3.4×10^{-2}	6.6×10^{-3}	2.74×10^{-2}	0.109

xenon lamp. The input power supply varied between −10 and +10 V, and resultant light and dark currents were measured. The attained current-to-voltage response curve of the pure and substituted thin films confirms the ohmic nature. The photoresponsivity (R_λ) is the photocurrent induced per unit power of the incident light on the exposed thin film area measured using eq 1.

$$R_\lambda = \frac{I_L - I_D}{(P_\lambda \times S)} AW - 1 \tag{1}$$

- P_λ is the intensity of the source
- S is the irradiated area
- I_D is the current under dark

- I_L is the current under light

The photoresponsivity and photocurrent of pure CGST and Fe-substituted CGST thin films are shown in Table 4. Generally, photocurrent performance mainly depends upon two characteristics: (1) Due to the IB, the increase in absorption of the below band-gap energy photons primes to the generation of the net electron−hole pair. (2) The generated electron−hole pair is collected as photocurrent at electrodes. This improvement in photocurrent production is because of two-step photon absorption, that is, the transition of the VB to the IB and from the IB to the CB. Research has been done on enhancing photocurrent using the IB from the direct transition of electrons of the parent material. From the results,
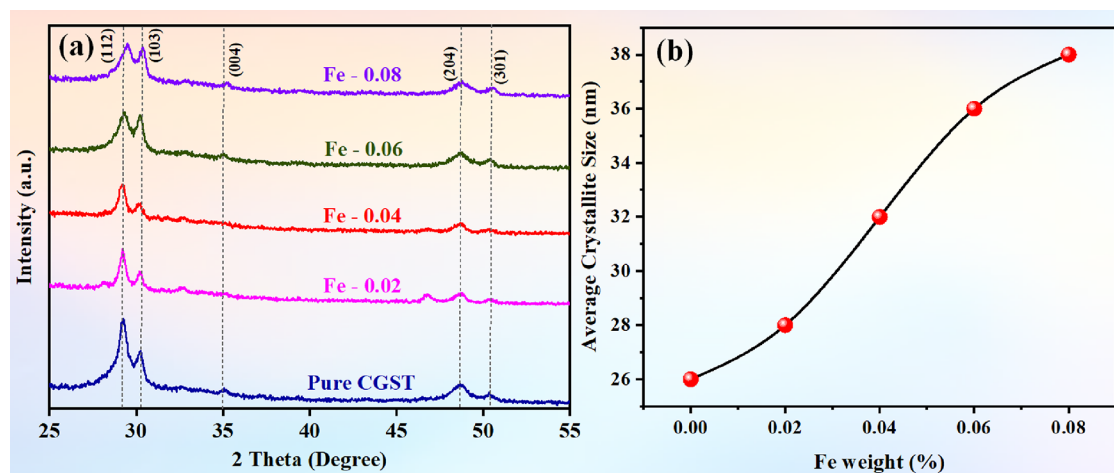
Figure 9. (a) X-ray diffraction pattern. (b) Average crystallite size vs. Fe concentration of pure CGST and Fe-substituted CGST thin films.

Table 5. Crystalline Size, d-Spacing, Lattice Constant Parameters, and Unit Cell Volume of Prepared Pure CGST and Fe: CGST Thin Films

sample name	crystallite size (nm)	d-spacing (Å)	lattice constant a (Å)	lattice constant c (Å)	dislocation density (lines/m^2) $\times 10^{14}$	unit cell volume (Å^3)
CGST pure	26	2.645	5.2917	10.7292	1.44	299.51
Fe 0.02	28	2.658	5.3228	10.8229	1.26	300.11
Fe 0.04	32	2.740	5.3279	10.9741	7.35	302.03
Fe 0.06	36	2.884	5.3542	11.2176	7.0	306.20
Fe 0.08	38	2.958	5.2917	10.7292	6.61	308.67

we can conclude that the enhancement of photoresponse due to the optical response of the IB makes multiple electron transitions in both pure and Fe-substituted thin films.

4.3. Structural Analysis. *4.3.1. X-ray Diffraction Analysis.* The XRD data were recorded for the deposited pure and Fe-incorporated CGST thin films, shown in Figure 9, and matched well with reference JCPDS # 01-085-1574. XRD of pristine and doped thin films consists of two prominent peaks at 29.1 and 30.5°, corresponding to the hkl values (112) and (103), respectively, and is indexed using Diffrac Eva and Origin software. The peaks at (112) and (103) approve the tetragonal structure of CGST, thus evidencing the formation of CGST. The XRD pattern exhibits a decrease in the intensity of diffraction peaks with an increase in concentration, demonstrating a reduction in crystallinity because of lattice distortion. While increasing the dopant concentration, the peak shifts slightly at lower angles. This shifting may be attributed to the smaller ionic radius of Ga (0.62 Å) compared with Fe (0.64 Å). No other secondary phases and impurity peaks, like Cu_2S and FeS, are observed. The lattice parameters of the deposited thin films are presented in Table 5. In the tetragonal system of the $CuGa_{1-x}Fe_x(S,Te)_2$, two Cu, one Ga, and one Fe ions are surrounded by S and Te ions as per our primary hypothesis (some Fe ions substitute, i.e., Ga ions). Due to this partial replacement, the S and Te ions move to the Fe ion position for an equilibrium.[21] The peak shift is due to the anion displacement. The change in anion displacement suggests that substituting a Ga site does not affect the CGST system.[11]

4.3.2. Raman Spectroscopy. The Raman spectra for pure and Fe-doped CGST thin films deposited at 300 ° C were analyzed. Chalcopyrite compounds typically have eight atoms per unit cell and 21 optical vibrational modes in the crystal structure.[22] The deconvoluted Raman spectra (Lorentzian fit) of pure and Fe-substituted CGST thin films are given in Figure

10a−e. The pure prepared films exhibited peaks at 302.05 cm^{-1}, which are attributed to the A_1 vibration mode, which signifies the vibration of S anions in the $x−y$ plane with cations at rest. The doped films in the vibrations in the range of 287.57−305.82 cm^{-1} and 348.92−354.49 cm^{-1} attributed to the A_{1g} mode are observed. The Raman spectrum affirms the purity of the deposited films, and no other secondary phase was present, which is in good agreement with powder XRD results. When the Fe dopant increases, the peak shift is observed toward the lower wavenumber. It is because of the electronegativity difference and mass of Fe and Ga ions. The electronegativity of Ga (1.81) is lower than the electronegativity of Fe (1.83). The intensity of the A_1 and A_{1g} vibration modes decreases with increasing the Fe dopant concentration.[23] Raman spectra were primarily based on the phenomenon of polarization associated with a concentration of dopant and the valency of the composition. Different vibration modes were obtained for Ga−S and Fe−S and are attributed to the substitution of Fe ions at the Ga ion site in the CGST material. Therefore, the vibration modes for Fe−S are more frequently associated with the anionic A_1 mode vibration. Additionally, the vibration mode A_{1g} peak explicitly confirms the incorporation of Fe ions into the pure CGST thin films.[2]

4.4. Surface Morphological and Elemental Composition Analyses. *4.4.1. Scanning Electron Microscopy.* The SEM micrographs of the surface morphology of pure and Fe-doped CGST thin films deposited at various concentrations of 0.02−0.08 are shown in Figure 11a−e. The deposited surface is observed as a mixture of rod- and sphere-shaped nanoparticles. The pure CGST thin film shows a mix of nanorods with nanosphere sizes around 244 to 355 nm. At 0.02 (Figure 11b), films were reduced to 2D rods and sphere nanostructures with sizes of 262 to 412 nm. Figure 11c,d shows a dense rod-like shape morphology of 334−867 nm diameter. These restate the
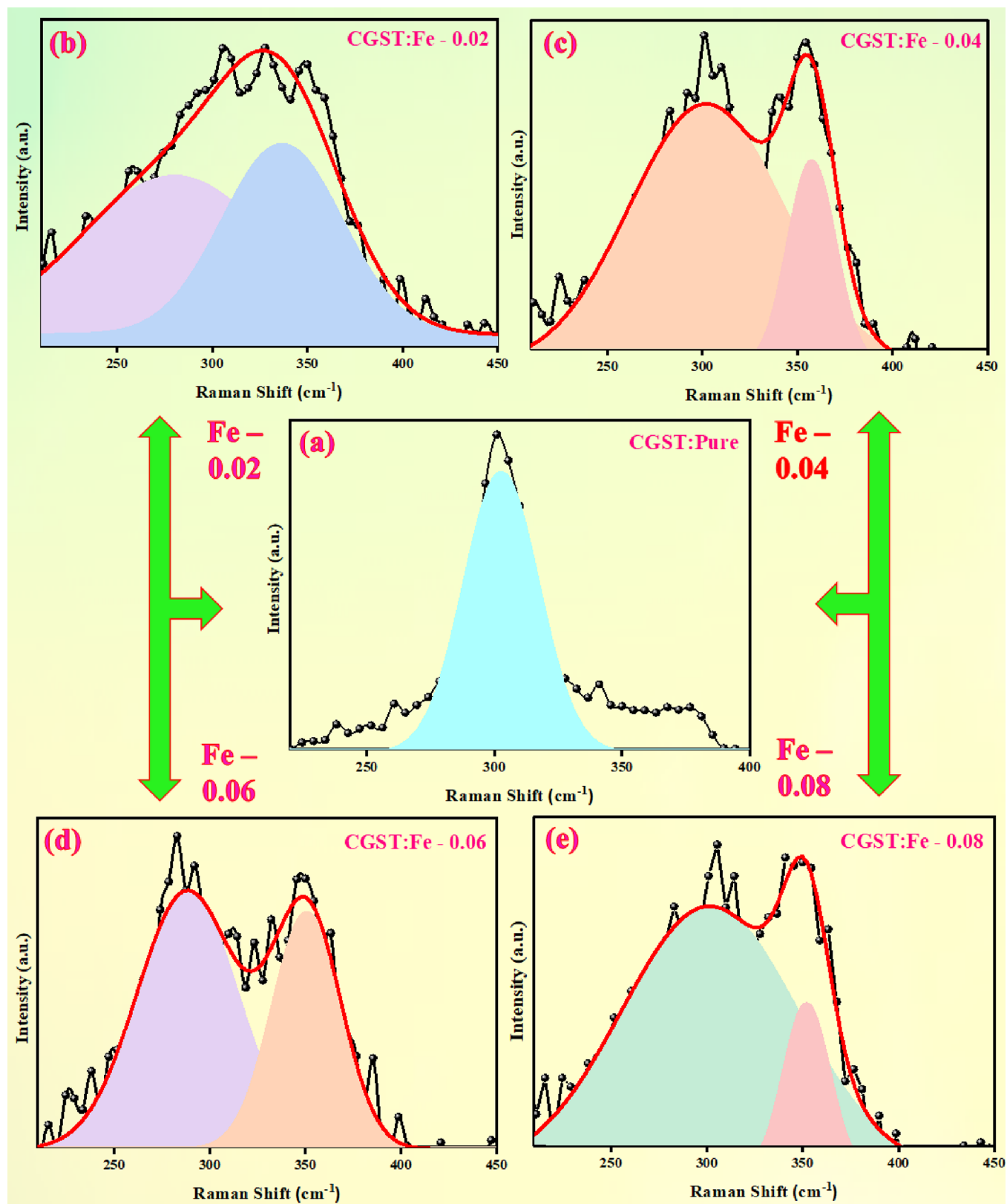
Figure 10. (a−e) Raman spectra for pure and Fe-substituted (0.02−0.08) CGST thin films.

various mechanisms (heterogeneous and homogeneous) involved in the spray coating in connection with doping per cent and deposition time. Due to the higher dopant concentration, Figure 11e shows the agglomerate surface morphology of the deposited thin films. Hence, the nanorod density is proportional to the Fe ion concentration and the development of CGST nanorods owing to the dopant. The particle size of the pure and Fe-doped CGST thin films slightly altered when increasing the dopant percentage. Hence, this research explains the growth mechanism of CGST thin films
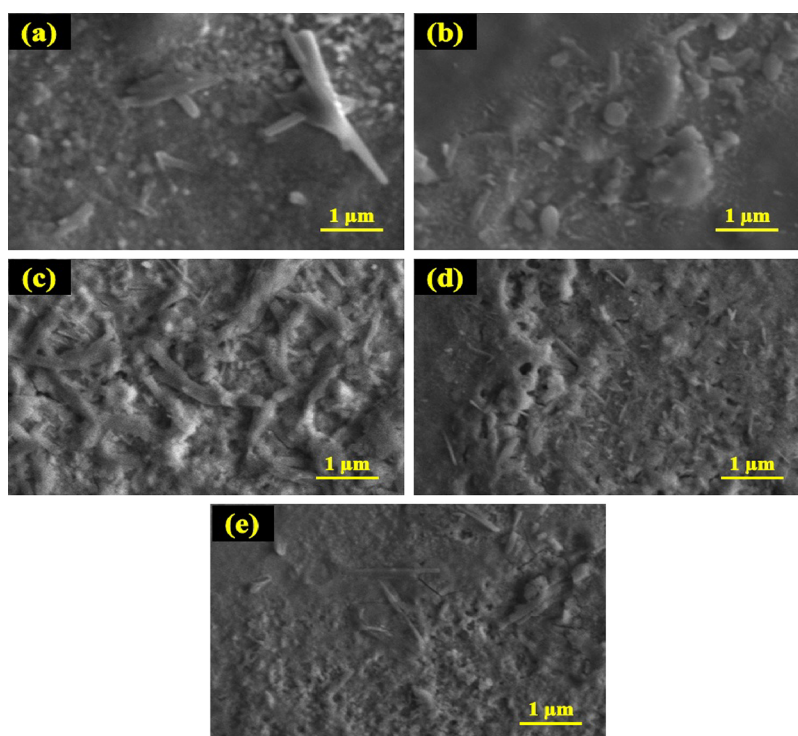
Figure 11. (a−e) SEM for pure and Fe-substituted (0.02−0.08) CGST thin films.
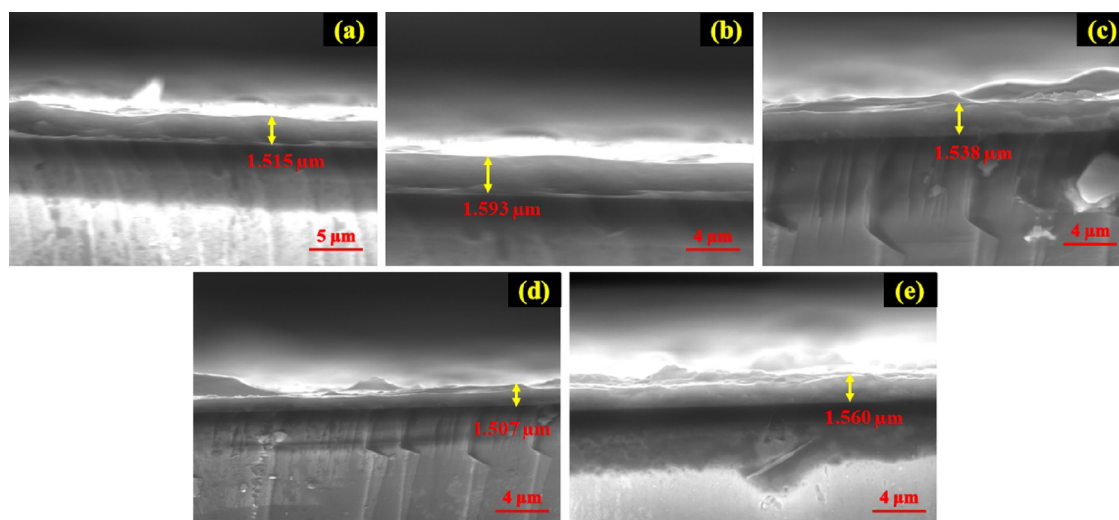

Figure 12. (a−e) Cross-section images for pure and Fe-substituted (0.02−0.08) CGST thin films.

compared to surface morphological changes by Fe substitution (Figure 12). Through the deposition of the precursor, the Fe ions interrelate with the pristine ions to form the films in connection with the temperature gradient on the surface of the substrate sustaining the primary homogeneous deposition mechanism. The conclusion is that the various Fe substitution concentrations considerably change the growth mechanism from the well-interconnected thin films to arbitrarily aligned CGST nanorods.[24] Figure 13 shows EDX mapping for the prepared pure and substituted CGST thin films, which confirms the existence of Cu, Fe, S, Te, and Ga in the deposited thin films. Figure 12a−e represents the cross-section images of pure and Fe-substituted (0.02−0.08) CGST thin films. The determined average film thickness is approximately 1.507 to 1.593 μm.

4.4.2. X-ray Photoelectron Spectroscopy. The elemental composition and oxidation state of the pure CGST and Fe-substituted CGST thin films via XPS are displayed in Figure 14. The XPS spectra reveal the existence of Cu 2p, Ga 3s, Ga 2p, S 2p, Te 3d, C 1s, and Fe 2p states, confirming all the elements in the deposited pure and substituted thin films.[26] The peaks were indexed and fitted by Casa software. For the Cu 2p plot, the peaks 934 and 936 eV are ascribed to the valence states of $Cu2p_{1/2}$, and $Cu2p_{3/2}$ energy levels agreed well with the same energy values for Cu^+ ions.[19] The result confirms that copper is in $a + 1$ oxidation state. The peaks observed at 1118 and 1145 are attributed to the binding energies of Ga $2p_{3/2}$ and Ga $2p_{1/2}$, respectively. The peak separation proved the trivalent state of Ga at 27 eV.[27] The binding energy of 161.5 eV corresponds to S 2p and has an S^{2-}
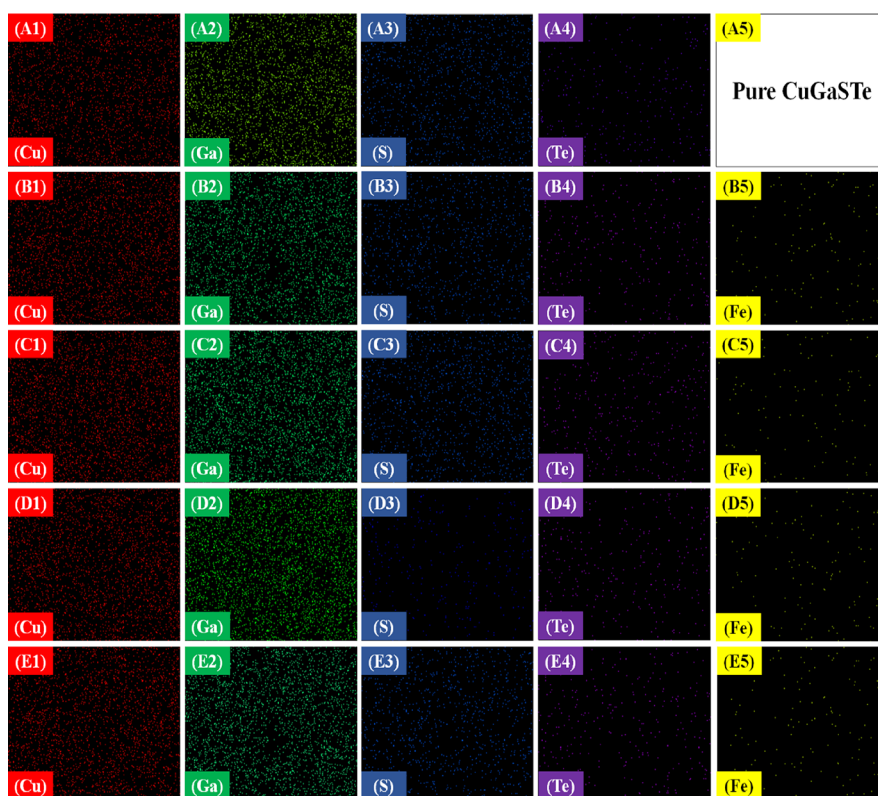
Figure 13. EDX mapping for the prepared pure and Fe-substituted CGST thin films.

oxidation state.[11] The peaks 725 and 711 eV affirm the Fe $2p_{1/2}$ and Fe $2p_{3/2}$ valence states of the Fe 2p spectrum. The Fe^{3+} and Fe^{2+} states exist at 716 eV, and these states have an energy difference between Fe $2p_{1/2}$; the Fe $2p_{3/2}$ state is 14 and 5 eV, correspondingly.[14] This study proposes the presence of Fe^{3+} and its substitution at Ga^{3+} sites of the CGST system. The estimated elemental composition from the XPS investigation for Fe-substituted $CuGa(S,Te)_2$ agreed well with EDAX measurement values. Hence, the oxidation states from the XPS study confirmed the partial substitution of Fe in the CGST system.

4.4.3. Atomic Force Microscopy. Figure 15a−e shows two-dimensional and three-dimensional (2D and 3D) morphological images of pristine and Fe-substituted CGST thin films. The pure and substituted films exhibit comparatively spherical nanoparticles deposited homogeneously throughout the substrate. We can detect that the substituted Fe plays a vital role in varying the size of the particle. The difference in particle size of the deposited thin films is owing to Fe^{3+} ion incorporation in the CGST lattice site. At 0.02 of Fe doping, the film shows the uniform distribution of nanoparticles, as in Figure 15b. The film images in Figure 15d,e display less spherical formation due to the higher substitution ratio of Fe (0.06 and 0.08). The line profile was calculated for a pure and Fe-substituted thin film, and a detailed study of average roughness properties was done. The calculated root mean square of roughness (RMS) values for pure CGST and Fe (0.02−0.08) are shown in Table 2. The reliable surface morphologies of pristine and Fe-doped thin films were confirmed by AFM and SEM studies. The study specifies the deposition of condensed and smooth thin films through the surface of the substrate.[24,25]

4.5. Modeling of CG$_{1−x}$Fe$_x$ST/In$_2$S$_3$ Heterojunction Solar Cells. The modeling was carried out via SCAPS 1D software, and the introduced experimental counterparts are shown in Table 1. The simulation relied on a two-layer heterojunction solar cell with an n-type In_2S_3 of 500 μm thickness and a p-type $CG_{1−x}Fe_xST$ of 1.5 μm and for window layer aluminum-doped zinc oxide (AZO) of 800 nm. The device's temperature was set constant to 523.15 K, respectively. The interfacial defect density between the layers of the $CG_{1−x}Fe_xST$ thin film and In_2S_3 is integrated with the simulation as 1015 cm$^{−3}$. Figures 16 and 17 display plots of the current density and quantum efficiency for simulated characteristics of $CG_{1−x}Fe_xST/In_2S_3$ heterojunction solar cells. Table 6 depicts the solar cell parameters from the simulation using SCAPS 1D software.[38−42] Fe-CGST was used to lessen the loss in the charge carrier to enhance solar cell efficiency. The modeled solar cell structure (glass/Fe-CGST/In$_2$S$_3$/AZO) is depicted in Figure 3. The prime aim of this study is to scrutinize the impact of electrical and optical characteristics after incorporation of the Fe layer (Fe-CGST). The simulation test was initiated with 0.02 of the Fe-CGST layer, and the concentration was varied up to 0.08. The results evidenced the correlative behavior of Fe and photovoltaic parameters in the simulated solar cell, as shown in Table 6. The increased photovoltaic attribute (J_{sc} and η (%)) with Fe incorporation can be attributed to the enhanced mobility of Fe-CGST, which was confirmed by the experimental results; this actively validates a decrease in the recombination rate of photo-generated charge carriers. The maximum efficiency is about 11.07% for 0.08 Fe-incorporated CGST.

4.5.1. Study on Current−Voltage Characteristics (J−V) and Quantum Efficiency (QE). The impact of Fe incorporation on the current−voltage plot (J−V) is depicted in Figure
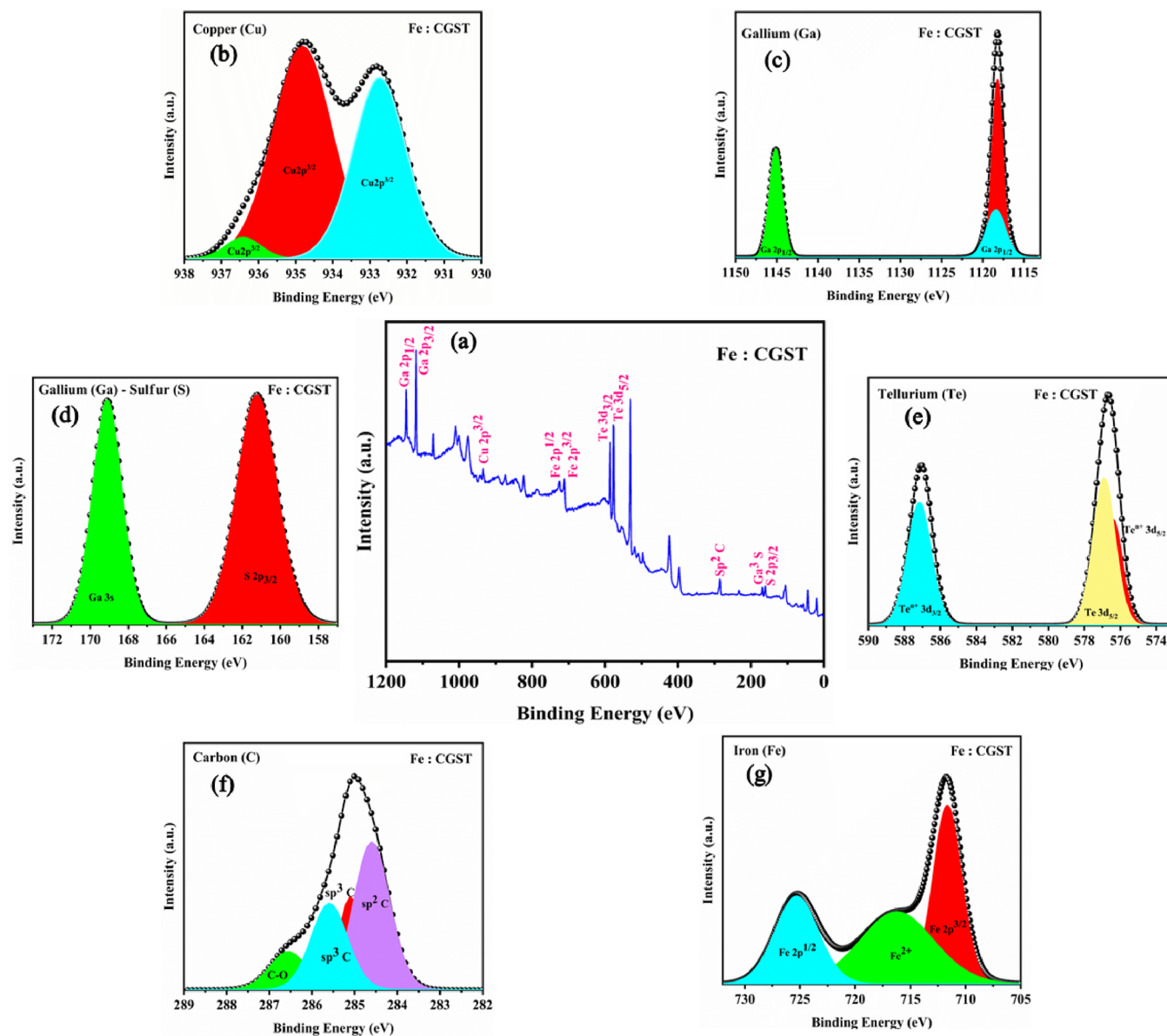
Figure 14. XPS data (a−g) for Fe 0.08 ratio-substituted CGST thin films.

17, and that on quantum efficiency (QE) is shown in Figure 16. The Fe-CGST layer, as the absorber layer of the solar cell, pointedly enhances the photovoltaic parameters of the investigated cell. With incorporation of the Fe-CGST layer, the open circuit voltage of the cell decreased from 1.46 to 0.90 V. The appropriate band alignment of Fe-CGST in the projected heterostructure will result in a higher integrated potential due to a higher band offset, hence decreasing the open circuit voltage.[43] The FF of the device went from 84.02% for the cell without Fe to 79.03% for the cell with Fe-CGST. This reduction can be understood by a decrease in the maximum power (Pm) produced by the solar cell. This enhancement in power is due to the incorporation of the Fe-CGST layer, which decreases the loss of recombination, which is agreed by the QE curves. These developments resulted in a notable rise in the photovoltaic η of the cell from 6.14 to 11.01% with 0 to 0.08 variation of Fe, which offered stability and appreciable charge carrier generation.

This specifies a new value in the numerical simulations of CIGS solar cell technology compared to recent articles.[44] The

solar cell has a strong absorption that reaches 100%, leading to a strong generation of electron−hole pairs with minimal reflection loss on the front face. For wavelengths less than 400 μm, the losses recorded in figure QE are probably due to the reflection on the front face. For wavelengths >1000 μm, a strong drop in quantum efficiency is observed due to the recombination losses on the rear face of the solar cell.[45]

5. CONCLUSIONS

An exertion of developing an IB absorber layer was put forward to encounter the research gaps in solar cells and flourished with unbeatable results compared to the reported literature. The tuning of optical and electrical attributes of CGST, which are key characteristics of solar cell material, was achieved by functionalizing CGST thin films using Fe substitution. The obtained enhancement is attributed to the formation of an IB that uses low-energy photons. Hall effect measurements confirm that the substitution ratio of Fe (0.02−0.08) gives a decrease in resistivity and carrier concentration and an increase in mobility and conductivity. The modeling was carried out via
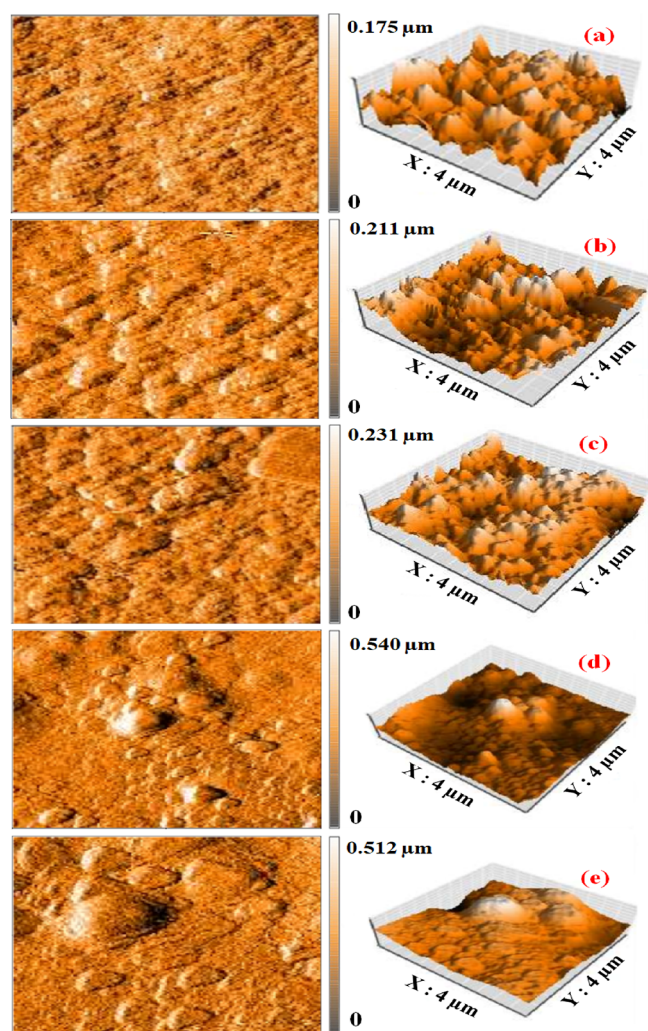
Figure 15. 2D and 3D AFM images of (a) pure, (b) 0.02, (c) 0.04, (d) 0.06, and (e) 0.08 of Fe-substituted CGST thin films.
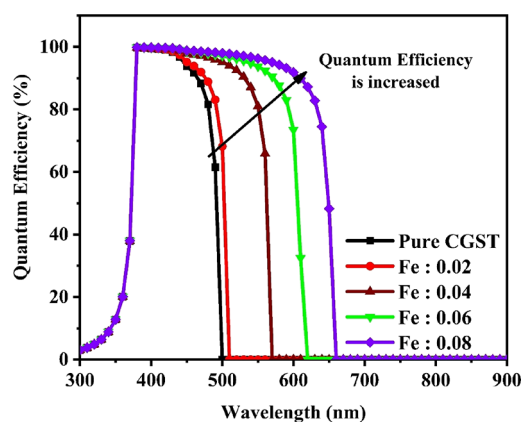

Figure 16. Quantum efficiency for $CG_{1-x}Fe_xST/In_2S_3$ heterojunction solar cells.

SCAPS 1D software, and solar cell characteristics were assessed. The $J–V$ characteristics of the $CG_{1-x}Fe_xST/In_2S_3$ heterojunction show an enhancement with the increase in Fe substitution. As the band gap of the thin film decreases, the rate of photon absorption increases and thereby the photo-excited electron–hole pairs in CIGS thin films increase. Thus, $CG_{1-x}Fe_xST$ solar cells have been suggested with 0.08 Fe
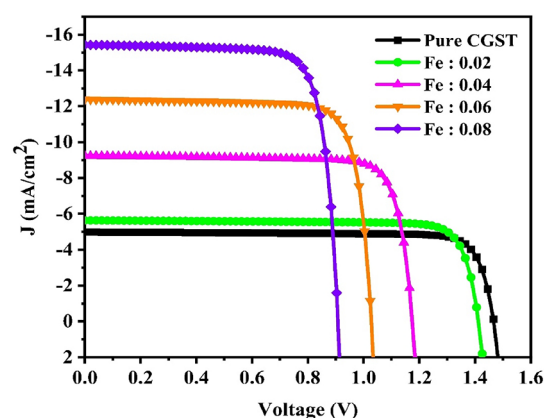

Figure 17. $J–V$ curve for $CG_{1-x}Fe_xST/In_2S_3$ heterojunction solar cells.

Table 6. Photovoltaic Parameters of $CG_{1-x}Fe_xST/In_2S_3$ Heterojunction Solar Cells

sample	V_{oc} (V)	J_{sc} (mA/cm^2)	FF (%)	efficiency (%)
pure CGST	1.46	4.98	84.02	6.14
Fe 0.02	1.41	5.63	83.69	6.66
Fe 0.04	1.17	9.23	81.90	8.88
Fe 0.06	1.02	12.38	80.42	10.24
Fe 0.08	0.90	15.42	79.03	11.07

substitution representing the highest J_{sc} and η values. Hence, from the theoretical simulation and experimental testing results, we conclude that the Fe substitution is a suitable material to create the IB in the CGST system, promising to enhance photovoltaic solar cell efficiency.

■ AUTHOR INFORMATION

Corresponding Author

Srikarumbur Pandurangan Vijayachamundeeswari − *School of Advanced Sciences, Vellore Institute of Technology, Vellore, Tamil Nadu 632014, India;* ⓘ orcid.org/0000-0002-9140-0995; Email: spvijaya.vit63@gmail.com

Authors

Karthikeyan Vijayan − *School of Advanced Sciences, Vellore Institute of Technology, Vellore, Tamil Nadu 632014, India*

Logu Thirumalaisamy − *Department of Physics, GTN Arts College, Dindigul 624005, India;* ⓘ orcid.org/0000-0002-0802-6219

Kalainathan Sivaperuman − *Centre for Nanotechnology Research, Vellore Institute of Technology, Vellore, Tamil Nadu 632014, India*

Nazmul Ahsan − *Research Center for Advanced Science and Technology (RCAST), University of Tokyo, Tokyo 113-0033, Japan;* ⓘ orcid.org/0000-0003-1311-1589

Yoshitaka Okada − *Research Center for Advanced Science and Technology (RCAST), University of Tokyo, Tokyo 113-0033, Japan*

Complete contact information is available at:
https://pubs.acs.org/10.1021/acsomega.2c08196

Notes

■ REFERENCES

(1) Vijayan, K.; Vijayachamundeeswari, S. P.; Sivaperuman, K.; Ahsan, N.; Logu, T.; Okada, Y. A review on advancements, challenges, and prospective of Copper and non-copper based thin-film solar cells using facile spray pyrolysis technique. *Solar Energy* 2022, 234, 81−102.

(2) Viveka, S. S.; Logu, T.; Ahsan, N.; Karthikeyan, J.; Murugan, P.; Sampath, M.; Sethuraman, K. Fe-doped CuGaS2 (CuGa1-xFexS2)-Detailed analysis of the intermediate band optical response of chalcopyrite thin films based on first principle calculations and experimental studies. *Mater. Sci. Semicond. Process.* 2021, 136, No. 106133.

(3) Shockley, W.; Queisser, H. J. Detailed balance limit of efficiency of p-n junction solar cells. *J. Appl. Phys.* 1961, 32, 510−519.

(4) Thirumalaisamy, L.; Ahsan, N.; Sivaperuman, K.; Kim, M.; Kunjithapatham, S.; Okada, Y. Engineering of sub-band in CuGaS2 thin films via Mo doping by chemical spray pyrolysis route. *Thin Solid Films* 2020, 709, No. 138252.

(5) Luque, A.; Marti, A. The intermediate band solar cell: progress toward the realization of an attractive concept. *Adv. Mater.* 2010, 22, 160−174.

(6) Gaur, A.; Khan, K.; Bhagat, B. R.; Sahariya, J.; Soni, A.; Dashora, A. Role of intermediate band and carrier mobility in Sn/Fe doped CuAlS2 thin film for solar cell: An ab-initio study. *Solar Energy* 2021, 215, 144−150.

(7) Pérez, L. M.; Aouami, A. E.; Feddi, K.; Tasco, V.; Abdellah, A. B.; Dujardin, F.; Feddi, E. M. Parameters Optimization of Intermediate Band Solar Cells: Cases of PbTe/CdTe PbSe/ZnTe and InN/GaN Quantum Dots. *Crystals* 2022, 12, 1002.

(8) Peng, W. H.; Li, B. B.; Shi, K. X., Chen, P. (2022). Analysis of the Metallic Intermediate Band in Cr-doped AgGaS2 Semiconductor for the Photovoltaic Application. In *Key Engineering Materials* (Vol. 920, pp. 172−178). Trans Tech Publications Ltd.

(9) Guillén, C.; Herrero, J. Influence of Cu content on the physical characteristics of CuxGaCr0. 1S2 thin films for intermediate band solar cells. *J. Mater. Sci.: Mater. Electron.* 2020, 31, 22398−22407.

(10) Fan, W.; Yao, H.; Wang, Y.; Li, Q. Structural and optical characteristics of Sn-doped CuGaSe2 thin films as a new intermediate band material for high-efficiency solar cells. *AIP Advances* 2020, 10, No. 065031.

(11) Lv, X.; Yang, S.; Li, M.; Li, H.; Yi, J.; Wang, M.; Zhong, J. Investigation of a novel intermediate band photovoltaic material with wide spectrum solar absorption based on Ti-substituted CuGaS2. *Solar energy* 2014, 103, 480−487.

(12) Conibeer, G.; Green, M.; Corkish, R.; Cho, Y.; Cho, E. C.; Jiang, C. W.; Lin, K. L. Silicon nanostructures for third generation photovoltaic solar cells. *Thin Solid Films* 2006, 511-512, 654−662.

(13) Vijayan, K.; Thirumalaisamy, L.; Qiu, R. F. J.; Kim, M.; Vijayachamundeeswari, S. P.; Sivaperuman, K.; Okada, Y. Enhanced Multifunctional Attributes of Tellurium Incorporated CuGaS2 Thin Films Employing Spray Pyrolysis Route. *Mater. Lett.* 2022, No. 132564.

(14) Han, M.; Zhang, X.; Zeng, Z. The investigation of transition metal doped CuGaS 2 for promising intermediate band materials. *RSC Adv.* 2014, 4, 62380−62386.

(15) Prabukanthan, P.; Dhanasekaran, R. Influence of Mn doping on CuGaS2 single crystals grown by CVT method and their characterization. *J. Phys. D: Appl. Phys.* 2008, 41, No. 115102.

(16) Chen, P.; Qin, M.; Chen, H.; Yang, C.; Wang, Y.; Huang, F. Cr incorporation in Cu G a S 2 chalcopyrite: A new intermediate-band photovoltaic material with wide-spectrum solar absorption. *Phys. Status Solidi A* 2013, 210, 1098−1102.

(17) Kalainathan, S.; Ahsan, N.; Hoshii, T.; Okada, Y.; Logu, T.; Sethuraman, K. Tailoring sub-bandgap of CuGaS2 thin film via chromium doping by facile chemical spray pyrolysis technique. *J. Mater. Sci.: Mater. Electron.* 2018, 29, 19359−19367.

(18) Martí, A.; Marrón, D. F.; Luque, A. Evaluation of the efficiency potential of intermediate band solar cells based on thin-film chalcopyrite materials. *J. Appl. Phys.* 2008, 103, No. 073706.

(19) Marsen, B.; Klemz, S.; Unold, T.; Schock, H. W. Investigation of the sub-bandgap Photoresponse in CuGaS2: Fe for intermediate band solar cells. *Progr. Photovolt.: Res. Appl.* 2012, 20, 625−629.

(20) Perednis, D.; Gauckler, L. J. Thin film deposition using spray pyrolysis. *J. Electroceram.* 2005, 14, 103−111.

(21) Mishra, S.; Ganguli, B. Effect of structural distortion and nature of bonding on the electronic properties of defect and Li-substituted CuInSe2 chalcopyrite semiconductors. *J. Alloys Compd.* 2012, 512, 17−22.

(22) Koschel, W. H.; Bettini, M. Zone-centered phonons in AIBIIIS2 chalcopyrites. *Phys. Status Solidi* 1975, 72, 729−737.

(23) Witte, W.; Kniese, R.; Powalla, M. Raman investigations of Cu (In, Ga) Se2 thin films with various copper contents. *Thin Solid Films* 2008, 517, 867−869.

(24) Logu, T.; Sankarasubramanian, K.; Soundarrajan, P.; Archana, J.; Hayakawa, Y.; Sethuraman, K. Vanadium doping induces surface morphological changes of CuInS2 thin films deposited by chemical spray pyrolysis. *J. Anal. Appl. Pyrolysis* 2016, 122, 230−240.

(25) Viveka, S. S.; Logu, T.; Ahsan, N.; Asokan, K.; Kalainathan, S.; Sethuraman, K.; Okada, Y. Study of sub-band states formation in the optical band gap of CuGaS2 thin films by electronic excitations. *J. Phys. Chem. Solids* 2022, 164, No. 110636.

(26) Lee, Y. S.; Cha, J. H.; Min, B. K.; Jung, D. Y. Electrophoretic deposition of Ga−Cu core−shell nanocomposites for CuGaS2 thin films. *Sol. Energy Mater. Sol. Cells* 2014, 125, 138−144.

(27) Okada, Y.; Morioka, T.; Yoshida, K.; Oshima, R.; Shoji, Y.; Inoue, T.; Kita, T. Increase in photocurrent by optical transitions via intermediate quantum states in direct-doped InAs/GaNAs strain-compensated quantum dot solar cell. *J. Appl. Phys.* 2011, 109, No. 024301.

(28) Luque, A.; Martí, A. Increasing the efficiency of ideal solar cells by photon induced transitions at intermediate levels. *Phys. Rev. Lett.* 1997, 78, 5014.

(29) Hashemi, J.; Akbari, A.; Huotari, S.; Hakala, M. Multi-intermediate-band character of Ti-substituted CuGaS 2: Implications for photovoltaic applications. *Phys. Rev. B* 2014, 90, No. 075154.

(30) Yoshida, K.; Okada, Y.; Sano, N. Device simulation of intermediate band solar cells: Effects of doping and concentration. *J. Appl. Phys.* 2012, 112, No. 084510.

(31) Abderrezek, M.; Djeghlal, M. E. Numerical study of CZTS/CZTSSe tandem thin film solar cell using SCAPS-1D. *Optik* 2021, 242, No. 167320.

(32) Benmir, A.; Aida, M. S. Analytical modeling and simulation of CIGS solar cells. *Energy Procedia* 2013, 36, 618−627.

(33) Khoshsirat, N.; Yunus, N. A. M.; Hamidon, M. N.; Shafie, S., Amin, N. (2013, September). ZnO doping profile effect on CIGS solar cells efficiency and parasitic resistive losses based on cells equivalent circuit. In *2013 IEEE International Conference on Circuits and Systems (ICCAS)* (pp. 86−91). IEEE.

(34) Qu, J.; Zhang, L.; Wang, H.; Song, X.; Zhang, Y.; Yan, H. Simulation of double buffer layer on CIGS solar cell with SCAPS software. *Optical and Quantum Electronics* 2019, 51, 1−14.

(35) Saha, S.; Rafique, M. Z. E., Hassan, M. S. (2016, January). Performance of CZTSxSe1− x solar cell with various mole fractions of sulfur for different buffer layers. In *2016 4th International Conference on the Development in the in Renewable Energy Technology (ICDRET)* (pp. 1−4). IEEE.

(36) Gezgin, S. Y.; Houimi, A.; Gündoğdu, Y.; Mercimek, B.; Kılıç, H. Ş. Determination of photovoltaic parameters of CIGS hetero junction solar cells produced by PLD technique, using SCAPS simulation program. *Vacuum* **2021**, *192*, No. 110451.

(37) Ghebouli, M. A.; Ghebouli, B.; Larbi, R.; Chihi, T.; Fatmi, M. Effect of buffer nature, absorber layer thickness and temperature on the performance of CISSe based solar cells, using SCAPS-1D simulation program. *Optik* **2021**, *241*, No. 166203.

(38) Khoshsirat, N.; Yunus, N. A. M.; Hamidon, M. N.; Shafie, S.; Amin, N. Analysis of absorber layer properties effect on CIGS solar cell performance using SCAPS. *Optik* **2015**, *126*, 681−686.

(39) Hamri, Y. Z.; Bourezig, Y.; Medles, M.; Ameri, M.; Toumi, K.; Ameri, I.; Voon, C. H. Improved efficiency of Cu (In, Ga) Se2 thinfilm solar cells using a buffer layer alternative to CdS. *Solar Energy* **2019**, *178*, 150−156.

(40) Al-Hattab, M.; Khenfouch, M.; Bajjou, O.; Chrafih, Y.; Rahmani, K. Numerical simulation of a new heterostructure CIGS/GaSe solar cell system using SCAPS-1D software. *Solar Energy* **2021**, *227*, 13−22.

(41) Za'Abar, F.; Zuhdi, A. W. M.; Bahrudin, M. S.; Abdullah, S. F.; Harif, M. N.; Hasani, A. H. (2018, August). Optimization of baseline parameters and numerical simulation for Cu (In, Ga) Se 2 solar cell. In *2018 IEEE International Conference on Semiconductor Electronics (ICSE)* (pp. 209−213). IEEE.

(42) Chakraborty, K.; Choudhury, M. G.; Paul, S. Numerical study of Cs2TiX6 (X= Br−, I−, F− and Cl−) based perovskite solar cell using SCAPS-1D device simulation. *Solar Energy* **2019**, *194*, 886−892.

(43) Husna, J.; Menon, P. S.; Chelvanathan, P.; Mohamed, M. A.; Tripathy, S. K.; Lenka, T. R. Numerical study of semi-transparent thin film heterojunction p-CuO/n-ZnO/AZO/ITO solar cells device model using SCAPS-1D. *Chalcogenide Lett.* **2021**, *18*, 667.

(44) Zhang, Y.; Shi, L.; Wang, Z.; Dai, H.; Hu, Z.; Zhou, S.; Zhang, Q. Silver-assisted optimization of band gap gradient structure of Cu (In, Ga) Se2 solar cells via SCAPS. *Solar Energy* **2021**, *227*, 334−342.

(45) Zheng, X.; Li, W.; Aberle, A. G.; Venkataraj, S. Efficiency enhancement of ultra-thin Cu (In, Ga) Se2 solar cells: optimizing the absorber bandgap profile by numerical device simulations. *Curr. Appl. Phys.* **2016**, *16*, 1334−1341.